JOURNAL OF SPACECRAFT AND ROCKETS
Vol. 33, No. 5, September–October 1996

In-Flight Flexure and Spin Lock-In for Antitank Kinetic Energy Projectiles

Ameer G. Mikhail*
U.S. Army Research Laboratory, Aberdeen Proving Ground, Maryland 21005-5066

A time-dependent analysis, coupling the rod vibration equation and pure roll motion equation, is formulated to numerically simulate the in-flight bending behavior of antitank kinetic energy projectile rods. The projectile is modeled as undergoing continuous, simulated planar pitching motion with the aerodynamic, spin, and structural damping forces included. The main parameter affecting the projectile spin and rod deflection responses is the fin torque producing the spin. Detailed spin, deflection, maximum stress, pitching angle, and rod shape histories are obtained along the projectile trajectory. Various steady-state spin cases are studied to simulate the effect of damaged fins. The spin lock-in phenomenon at the first lateral flexing natural frequency is captured by the present model for rods with simulated damaged fins. Any deformable projectile attempting, because of damaged fins, to spin past that frequency was found to lock-in to spinning at that frequency. Both sub- and supercritical spin cases are computed. Predictions of the rod shape at any instant and under actual flight conditions are made.

Nomenclature

A_{ref} = reference area, $(\pi d^2/4)$, in.^{2}
$A(x, t)$ = aerodynamic force normal to the x axis, per rod unit length, $(\partial C_{N\alpha}/\partial x) \cdot \alpha_{\text{eff}} \cdot (q \cdot A_{\text{ref}}) \cdot \cos(\alpha_b)$, lbf/in.
C_D = drag coefficient, drag force/$(0.5\rho_\infty V_\infty^2 A_{\text{ref}})$
C_l = rolling moment coefficient, $l/(q_\infty A_{\text{ref}} d)$
C_{lI} = induced roll moment coefficient, resulting from the cyclic fin loading at angle of attack identical to induced roll moment/$[q_\infty \cdot A_{\text{ref}} \cdot d \cdot \sin(n\lambda)]$
C_{lo} = projectile trim roll moment coefficient
C_{lp} = roll moment damping coefficient derivative, $\partial C_l/\partial(pd/V)$, per rad
$C_{l\delta}$ = fin produced roll moment coefficient derivative, $\partial C_l/\partial\delta$, per rad
C_N = normal force coefficient, normal force/$(q_\infty A_{\text{ref}})$
$C_{N\alpha}$ = normal force slope coefficient, $\partial C_N/\partial\alpha$, per rad
c = rod structural damping coefficient, per rod unit length $[0.002c_{\text{crit}} \equiv 0.002\sqrt{(mk)}]$
d = projectile reference diameter, in.
E = Young's modulus of elasticity, psi
I = area moment of inertia for the rod cross section about the neutral axis passing through the section centroid, in.^{4}
I_x = axial (polar) moment of inertia about the body instantaneous spin axis, lb-in.^{2}
I_y = transverse moment of inertia about an axis passing through the body center of mass, lb-in.^{2}
k = rod spring stiffness per unit rod length, (lbf/in.)/in.
L = total length of the projectile, in.
l = roll moment, in.-lbf
M = Mach number of the projectile
m = rod mass per unit length, lb/in.
n = number of fins in a fin set
p = spin rate of projectile, rad/s (except when noted in Hz)
p_s = steady state spin rate, Hz
q = dynamic pressure, $(0.5\rho V^2)$, psi
$S(x, t)$ = spin centrifugal force per unit rod length, $m \cdot p^2 \cdot (y \cdot |\cos(p \cdot t)|)$, lbf/in.
t = time, s
V = projectile velocity, ft/s
α_a = rigid body pitching angle of attack, deg
α_b = local body segment slope, $\partial y/\partial x$, deg
α_{eff} = local effective angle of attack, $\alpha_a - \alpha_b$, deg
δ = fin cant angle for a whole fin panel, deg
δ_p = partial fin cant angle (chamfer) at the leading and/or trailing edge of the fin panel, deg
δ_{eq} = equivalent whole panel fin cant angle for the partially canted (chamfered) fin, deg
λ = fin roll orientation angle with respect to the plane of angle of attack, deg
ρ = air density, lb/in.^{3}
ϕ = roll angle, radian
$\dot{\phi}$ = roll (spin) rate, $d\phi/dt = p$, rad/s (except when noted in Hz)
$\ddot{\phi}$ = $d\dot{\phi}/dt$, rad/s^2

Introduction

LONG kinetic energy (KE) rods are known to occasionally flex during flight, perhaps because of some mass eccentricity and high off-design spin produced by damaged fins. Some rods exhibit bent shapes very near the gun muzzle resulting, perhaps, from the high launch impulse load and the sabot/gun-tube dynamic interaction, as depicted in Fig. 1. However, in most cases known of rod flexure, the rod starts out straight at the muzzle then it starts to bend, leaving distinguished imprints on cardboard and wire screens placed at 1 and 3 km, as shown in Fig. 2.

Although theoretical and numerical models for in-flight rod flexing have been attempted and presented in some published and

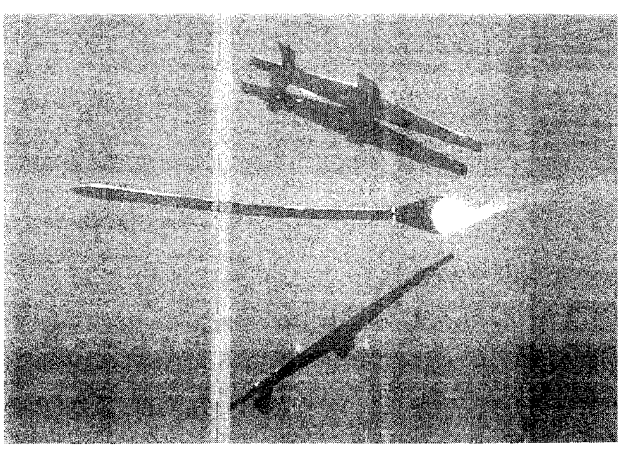

Fig. 1 Subcaliber KE rod bent at launch.

Presented as Paper 95-3429 at the AIAA Atmospheric Flight Conference, Baltimore, MD, Aug. 7–9, 1995; received Sept. 1, 1995; revision received April 27, 1996; accepted for publication May 6, 1996.

*Aerospace Engineer, Propulsion and Flight Division, Weapons Technology Directorate. Associate Fellow AIAA.

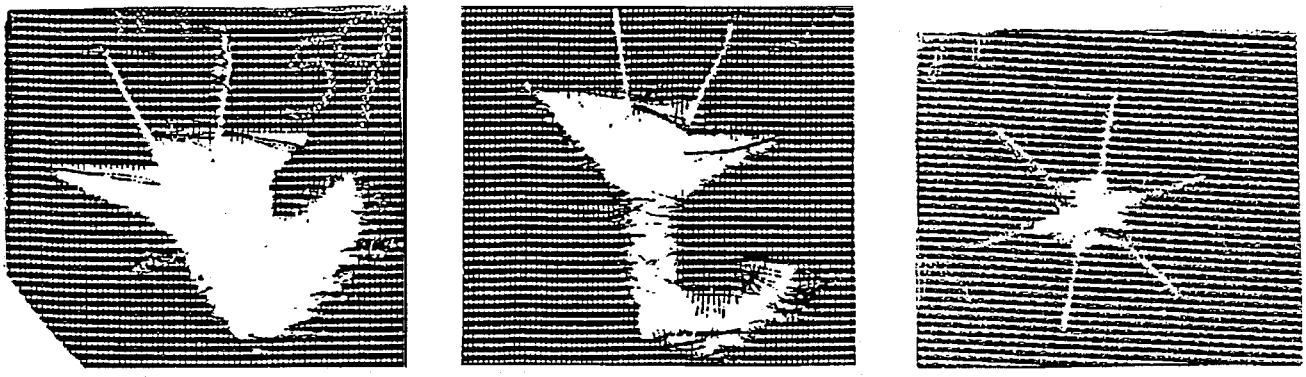

1-km imprint | 3-km imprint | 1-km imprint from a properly flying round

Fig. 2 Screen imprints from live firing, indicating rod bending.

unpublished work,[1–9] many have not fully disclosed their detailed analyses[1–3] nor applied them to real-life test cases.[7] The present analysis is the first to provide a direct approach to this complex in-flight phenomenon, which is becoming increasingly important because of the trend in designing longer and slimmer antitank penetrators.

It is desired to be able to predict the spin and deflection history at any time in flight for a given projectile under given flight conditions. Reference 1 comes closest in providing such results; however, details of its modified 6-degree-of-freedom (6DOF) analysis, the structural equation, and all of the assumptions are not available for verification or review (proprietary in nature). References 2 and 3 provide some results using an nDOF code ($n = 8$), but again no details are given of the model for review and/or application. References 4 and 5 provide simplified analysis for a possible steady-state spin effect on reducing the natural resonance frequency from its nonspinning value. Reference 6 considered conservation of rotational momentum for a rod with spin by tracking the increase in axial moment of inertia and deducing the spin value from the conserved moment product (axial moment of inertia times the spin rate). This approach does not provide time history nor does it include the aerodynamic and structural damping forces. All of the simplistic approaches wrongfully predict that once the rod is spun at, or near, the natural frequency, the rod will bend indefinitely until it breaks.

Other than that of Ref. 1, no model has indicated the spin lock-in behavior or shown realistic time histories along the flight path. Reference 7 presented analytic solutions to the present rod vibrational problem for a concentrated fin force but no centrifugal force or instantaneously varying spin rate. Its analysis also suffers from sensitivity and unacceptable limitations on permissible initial rod shapes. References 8 and 9 presented approaches for another interesting problem, which pertains to rod spin lock-in at the low frequency of the pitching motion. The latter problem is not a rod-flexing or a structurally related problem but rather a three-dimensional motion problem where the pitching and yawing motions become strongly coupled and resonate. This spin/pitch-frequency lock-in problem will not be addressed. The present work deals with in-flight flexture and its effect on the roll motion. The roll motion equation is coupled to the beam deflection equation of a free/free rod. The two equations are then solved numerically.

Analysis

Coordinates

For the curved rod body (Fig. 3), the body-fixed coordinates with regard to a reference direction in space are as follows. The x axis is the principal axis passing through the center of mass of the rod at each instant. The y axis is perpendicular to the x axis and is located at the rod tip end. The instantaneous spin axis for the bent rod is the x axis.

Approach

The elastic beam vibration equation subjected to the external aerodynamic normal force and the spinning centrifugal force, together with the internal structural damping force, is solved together with the pure roll motion equation (with time varying axial moment of inertia). The body is assumed having an initial deflection curve (providing a mass offset); then the aerodynamic, spin, and structural damping forces are applied in the free/free beam equation to yield a new rod shape. A new axial moment of inertia is computed for the new shape and then fed to the pure roll motion equation, with updated aerodynamics, to yield a new spin rate, which is then fed to the structural equation with all updated forces. The same cycle is then repeated for each time step. As time proceeds during flight, the projectile slows because of drag and a new velocity is obtained from a built-in trajectory retardation equation solution. The velocity and roll producing and roll damping moment derivative coefficients are computed each time, from a provided aerodynamic data table obtained from range tests. During 1 s of flight, the projectile under study (shown in Fig. 4) will decelerate from $M = 5.3$ to about 4.7, with very small variation in the normal force derivative coefficient ($C_{N\alpha}$). Therefore, for computation simplification, the normal force coefficient and its distribution along the body were considered unchanged during this short flight, and the normal force at each body segment was computed based on the local body curvature and the local angle of attack, as defined in Fig. 3. The normal force distribution on the body was computed using the fast aerodynamic design code of Ref. 10 and is provided in Fig. 5 for Mach number of 5.5 and $\alpha = 2$ deg. The moment distribution resulting from this normal force is small and was not included, as also justified in Ref. 1, for simplifying the computations.

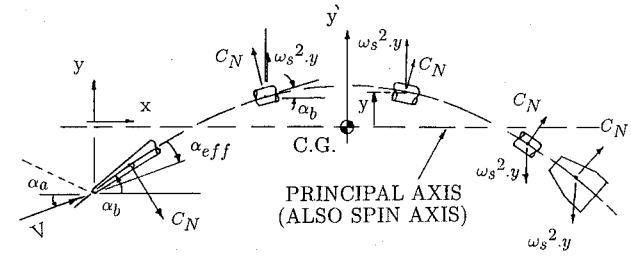

Fig. 3 Coordinates and general nomenclature: $\alpha_a = \alpha_0 \cos(\omega_p \cdot t)$ and $\alpha_{eff} = \alpha_a - \alpha_b$.

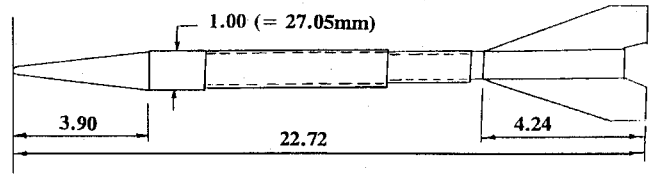

Fig. 4 Geometry of the subcaliber KE projectile: dimensions in calibers.

Governing Equations

Pure Roll Motion Equation

The pure roll motion equation can be written as

$$\frac{\mathrm{d}(I_x\dot{\phi})}{\mathrm{d}t} = q \cdot A_{\mathrm{ref}} \cdot d \cdot \left[C_{lo} + C_{l\delta} \cdot \delta + C_{lp}\frac{\dot{\phi}\, d}{V} - C_{ll} \cdot \sin(n\lambda) \right] \tag{1}$$

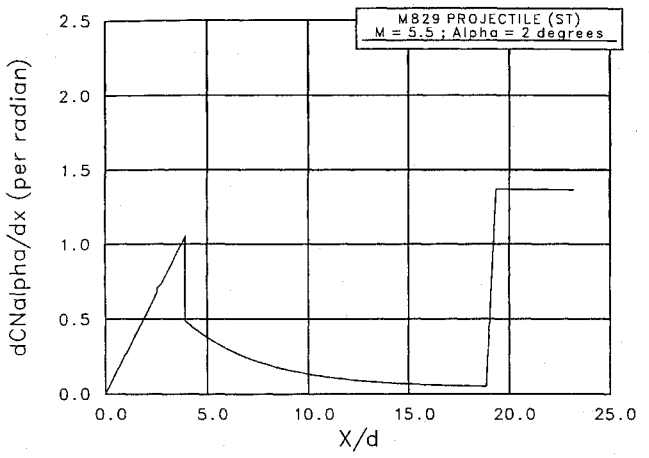

Fig. 5 Aerodynamic force load on the projectile, normal force slope coefficient per unit length.

subject to the initial condition

$$\dot{\phi} = \dot{\phi}_0 \qquad \text{at } t = 0 \tag{2}$$

This equation is solved as a first-order equation in $\dot{\phi}$. The value $p = \dot{\phi}$ is then used to provide the spin centrifugal force in the elastic-beam equation. The trim roll moment value is random from round to round, and can be either positive or negative. The induced roll moment is considered small for the high spin rates considered here; also, no values were measured or available. Therefore, both moment coefficients were taken as zero. Both $C_{l\delta}$ and C_{lp} were made functions of α_{eff} to account for the large rod deflection. Both were made to increase quadratically with α_{eff} up to $\alpha_{\text{eff}} = 10$ deg and then decrease quadratically to $\alpha_{\text{eff}} = 20$ deg and beyond, as suggested by wind-tunnel results.[11] C_{lp} was increased to 130% at 10 deg (from its value at 0 deg) and to 117% at 20 deg. Similarly, $C_{l\delta}$ was increased to 110% at 10 deg and decreased to 87% at 20 deg.

Elastic Rod Equation

Considering the shear and rotary inertia forces to be of second order in the beam deflection equation, the beam vibration/deflection equation, can be written as

$$\frac{\partial^2(EIy''/a)}{\partial x^2} + m\frac{\partial^2 y}{\partial t^2} + c\frac{\partial y}{\partial t} = A(x,t) + S(x,t) \tag{3}$$

where

$$y'' = \frac{\partial^2 y}{\partial x^2}, \qquad a = 1 + (y')^2, \qquad y' = \frac{\partial y}{\partial x}$$

The sign for the forces are taken to be consistent with the signs of the chosen coordinate system, i.e., positive normal force is in the direction of positive y.

Equation (3) is subject to the free/free boundary conditions, reflecting zero bending moment and zero shear force at both rod ends, i.e.,

$$\left(\frac{EIy''}{a}\right) = 0, \qquad \text{or} \qquad y'' = 0 \tag{4}$$

at both $x = 0$ and $x = L$, and

$$\frac{\partial(EIy''/a)}{\partial x} = 0, \qquad \text{or} \qquad y''' = 0 \tag{5}$$

at both $x = 0$ and $x = L$. The term a was included in the equation to account for large deflection and large rod curvature to yield more accurate results.

The rod was considered as a rigid body undergoing a pitching motion. The rigid-body planar angle of attack can be modeled as in damped or undamped pitching motion using

$$\alpha(t) = \alpha_0 \cos(\omega_p t) e^{-0.693t} \tag{6}$$

or

$$\alpha(t) = \alpha_0 \cos(\omega_p t) \tag{7}$$

respectively. The initial pitching angle α_0 was taken to be 4 deg and the pitching motion frequency ω_p was 20 Hz. The damped pitching angle model of Eq. (6) was used, providing an $\alpha = 0.5\alpha_0$ at 1 km from the gun muzzle.

Case Study

First, calculations were initiated and performed to simulate the case of a subcaliber projectile that has an L/d of 22.72, as shown in Fig. 3. The aerodynamic coefficients were obtained from the U.S. Army Research Laboratory indoor transonic range test database. In the enclosed range the tests are made on steel models rather than on the actual depleted uranium (DU) rounds for safety considerations. Therefore, simulations were also made for that particular material. The relevant information regarding this configuration is given in Table 1.

The first lateral flexing natural frequency (FNF) of the rod was estimated using Ref. 12. The corresponding theoretical value for a uniform rod was 323 Hz. The difference is because of both nose and fin mass and bending stiffness deviation from a uniform bar. The corresponding value for a uniform DU rod is 207 Hz. The structural damping constant was used as 0.2% of the rod critical damping value, as also used in Ref. 1 and later measured and reported in Ref. 13, which is a memorandum letter carrying values of measured flexural structural damping. The spring-stiffness distribution for a free/free rod, under end transverse loads, was shown to be similar to that of a simply supported beam.[14] However, a spanwise constant spring value was used here, so as not to influence the rod bending solution toward the first natural mode shape (which resembles a shifted deflection curve for a simply supported beam).

Computations were made for 10 cases with different steady-state spin values for the given configuration, covering the spectra of sub- and supercritical spin as well as the effects of initial rod shape and rod structural damping. The different steady-state spin cases were considered to reflect the effect of various damaged fins. The actual equivalent fin cant angle was 0.55 deg, resulting in a steady-state spin of 90 Hz. Table 2 provides the fin cant angles used to simulate damaged fins, and the corresponding steady-state spin values.

Table 1 Physical properties of the projectile

Reference diameter, in. = 1.06
$L/d = 22.72$
Material = steel
E, lbf/in.$^2 = 30 \times 10^6$
Mass, lb = 4.281
Ix, lb-in.$^2 = 0.6956$
Iy, lb-in.$^2 = 143.56$
Launch speed, ft/s = 5905.8
Launch spin, Hz = 0
FNF, Hz = 380

Table 2 Cases simulated

Case no.	Description	Equivalent fin cant angle, deg	Steady-state spin, Hz
1	Undamaged fins	0.55	90
2	Damaged fins	1.65	270
3	Damaged fins	2.20	360
4	Damaged fins	2.32	380
5	Damaged fins	2.44	400
6	Damaged fins	2.75	450
7	Damaged fins	4.40	720
8	Undamaged fins (with high launch spin, 600 Hz)	0.55	90
9	Damaged fins (with large, 1.00%, structural damping)	1.65	270
10	Damaged fins (with different initial rod shape)	4.40	720

These chosen high spin values were purposefully selected so as to provide answers about structural behavior near and through the FNF and to investigate the spin/flexural frequency lock-in phenomenon. The critical spin is defined as the spin where resonance occurs, which is usually at or above the FNF (because of the small structural damping). Spin was suggested to slightly lower the resonance frequency from its FNF value.[4,7]

Computations

Computations were made using 51 uniform body segments. The actual mass, material properties, and rod area moment of inertia distributions along the rod were used to reflect the real projectile, rather than a uniform rod. Finite differences were used to solve both equations. Very small time steps ($\Delta t = 1.5 \times 10^{-6}$ s) were necessary to capture any high-frequency changes in deflection or spin histories, and for numerical stability. The run time on a minicomputer (SGI-Challenge XL/R4400) is about 40 min for the 1 s of flight time, using one processor. The corresponding case of a rigid, inelastic body takes about 40 s for the same 1 s time of flight.

Deflection Equation

Finite differences were used to solve both Eqs. (1) and (3). Equation (3) was solved first; then Eq. (1) was solved at every time step. Care must be given in solving Eq. (3), which is very sensitive to differencing accuracy and can result in wrong deflection and higher resonance frequency. The same remark applies to the boundary conditions of Eqs. (4) and (5). Second-order accuracy in time and fourth order in space were needed to obtain the results. Only three time-level computer storages were needed for the large number of time steps required to compute results to the 1 s real time of flight. The calculations were made on a 32-bit machine, corresponding to double precision on older 16-bit mini and mainframe machines. Equation (3) was written, for each point on the rod, at time n, as

$$\frac{m(y_{n+1} - 2y_n + y_{n-1})}{\Delta t^2} + \frac{c(y_{n+1} - y_{n-1})}{2\Delta t} = F(x, t)$$

then the solution y_{n+1} becomes

$$y_{n+1} = \frac{F(x,t) + m(2y_n - y_{n-1})/\Delta t^2 + cy_{n-1}/2\Delta t}{m/\Delta t^2 + c/2\Delta t}$$

The initial condition $(\partial y/\partial t)\,|_{t=0} = v_0$ was applied at $t = 0$, with v_o value taken as 4 ft/s. The first term in Eq. (3) needed careful treatment because it is the main influencing term in that equation. Each rod segment was represented by a point i placed at its centroid. A seven-point formulation, in conservative form, was found necessary to provide satisfactory accuracy. This term was written as

$$\left.\frac{\partial^2 (EIy'')}{\partial x^2}\right|_i = \frac{(EIy'')_{i+1} - 2(EIy'')_i + (EIy'')_{i-1}}{\Delta x^2} - \left(\frac{\Delta x^2}{12}\right)(EIy'')_i^4 + \mathcal{O}(\Delta x^4) \tag{8}$$

where

$$(EIy'')_i^4 = \frac{(EIy'')_{i+2} - 4(EIy'')_{i+1} + 6(EIy'')_i - 4(EIy'')_{i-1} + (EIy'')_{i-2}}{\Delta x^4} + \mathcal{O}(\Delta x^4)$$

where

$$y_i'' = \frac{8y_{i+3} - 108y_{i+2} - 1080y_{i+1} + 1960y_i - 1080y_{i-1} - 108y_{i-2} + 8y_{i-3}}{725\Delta x^2} + \mathcal{O}(\Delta x^6)$$

The conservation form expansion of $[(EI)y'']''$ in Eq. (8) was found to be necessary to preserve the accuracy of differencing, rather than the equivalent nonconservative form

$$(EI)y^4 + 2(EI)'y''' + (EI)''y''$$

The variation in the product (EI) along the rod configuration, mainly at the nose and tail sections, was important in providing the resultant resonance frequencies. The tail section is usually made of aluminum. If this variation is not included, or inadequately differenced, it will result in inaccurate natural and resonance frequencies as well as larger deflection for the rod.

Note that the deflection equation is coupled to the roll equation only through the spin variable p ($\equiv \dot{\phi}$). However, this coupling is very influential on the deflection solution.

Treatment of Boundary Conditions

The fourth-order Eq. (3) has four boundary conditions. This requires the specification of two end points at each end of the rod. Each rod segment is represented by a point at its centroid. Since both y'' and y''' are zero at both end points, $y'|_{x=0}$ (or, alternatively, $y = c_1 x + c_2$) is found to be the exact solution as $x \to 0$. Thus linear extrapolation from points 4 and 3 to points 2 and 1 along the rod body was found to be the most accurate and numerically stable form. Extrapolation was made also to account for the variation in area moment of inertia, which is largest at each rod end. Failure to include this variation will lead to erroneous and larger deflection. The final form derived for the two point boundary conditions is

$$y_2 = \frac{(7A_1 - 5A_3)y_3 - 5(A_4 + A_1)y_4}{5A_2 + 11A_1}$$

and

$$y_1 = \frac{y_4 - 7y_3 + 11y_2}{5}$$

where

$$A_1 = 4I_2 - 3I_1, \qquad A_2 = -8I_2 + 6I_1 - I_3$$
$$A_3 = 4I_2 - 3I_1 + 2I_3, \qquad A_4 = -I_3$$

where I_1, I_2, and I_3 are the area moments of inertia at points 1, 2, and 3 on the rod, respectively. The rod other end boundary conditions at $x = L$ are similarly derived.

Roll Equation

The roll equation [Eq. (1)] was solved as a first-order equation in $\dot{\phi}$, with the boundary condition given by Eq. (2). Equation (1) was written as

$$(I_x\ddot{\phi})_n + (\dot{I}_x\dot{\phi})_n + BB\dot{\phi}_n + CC = 0$$

The solution $\dot{\phi}_{n+1}$ was then computed as

$$\dot{\phi}_{n+1} = \dot{\phi}_n - \Delta t \frac{(\dot{I}_x\dot{\phi})_n + BB\dot{\phi}_n + CC}{(I_x)_n}$$

The roll equation is coupled to the rod deflection equation through the terms I_x and $\dot{I}_x$, which are computed each time step, based on the rod shape resulting from the deflection equation.

Results

Computations were first made for an ideal rod of infinite rigidity (very large E, resulting in zero body deflection) and perfectly straight rod geometry, with different fin damage cases (the first seven cases of Table 1). For these ideal conditions, the rod spun through the critical natural frequency, as expected, without any spin lock-in or resonance. The spin histories for these cases are shown in Fig. 6. The ability to be spun past the FNF is a common feature for power shafts, which are usually of higher stiffness (smaller L/d), more precisely manufactured (less eccentricity), and have active balancing mechanisms that keep them almost perfectly straight.

Computations were then repeated for the real rod of a deformable body and with initial bent geometry. A bent shape of a sine curve was chosen with a maximum midpoint sag of 0.35 in., thus providing tip and tail end deflections of −0.22 in. and a midrod deflection of +0.13 in. Also a case of an initial shape resembling the second bending mode, with the same midsag of 0.35 in., was computed. The flight range/time trajectory was computed for the given projectile. It indicated that at the 1-s flight time mark, the projectile would have reached about 5578 ft (1700 m).

Results for the given projectile are discussed next. Figure 7 depicts the spin history for the design projectile with no fin damage. Small oscillations are present, reflecting the change in I_x because of the change in rod shape. These oscillations are dampened out because of the structural damping. The tip segment deflection, initially at 0.22 in., is shown to decrease to 0.05 in. at $t = 0.9$ s, as given by Fig. 8. The pitching angle of the tip segment, for the damped pitching motion, is given in Fig. 9. It shows the high frequency of flexing is reflecting itself on the low pitching motion frequency of 20 Hz. It also shows an angle amplification to about 6 deg from an initial value of 4 deg, for $t < 0.10$ s. The maximum stress in the rod is also computed at the outer fiber at the midrod point, based on the rod curvature at each instant. Figure 10 indicates that a stress of ±100,000 psi at the muzzle is reduced to about ±30,000 psi at $t = 0.9$ s, because of damped rod deflection.

For spin-up cases with steady-state spin close to (but lower than) the FNF, the rod starts to exhibit larger deflection and larger spin oscillation along its trajectory. However, no spin lock-in occurs. This is illustrated by the spin history of the case of 360-Hz spin, depicted in Fig. 11. This behavior also continued for the case of 380 Hz, which is estimated to be the theoretical FNF, as shown in Fig. 12. No spin lock-in occurred, and the tip deflection was relatively large and did not dampen out quickly, as given in Fig. 13.

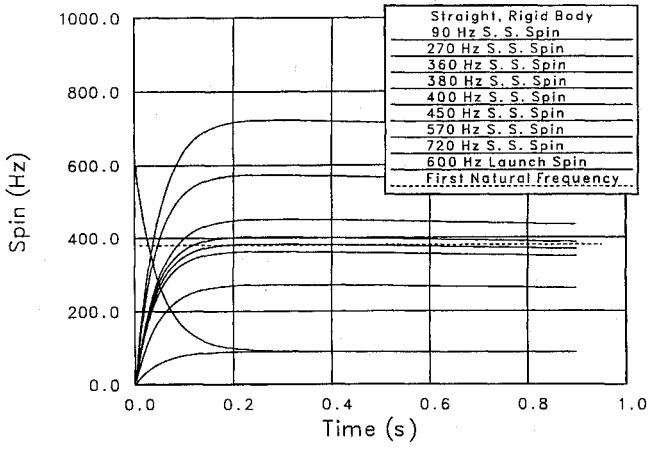

Fig. 6 Straight, undeformable projectile rod spin history: 120-mm subcaliber KE projectile (steel).

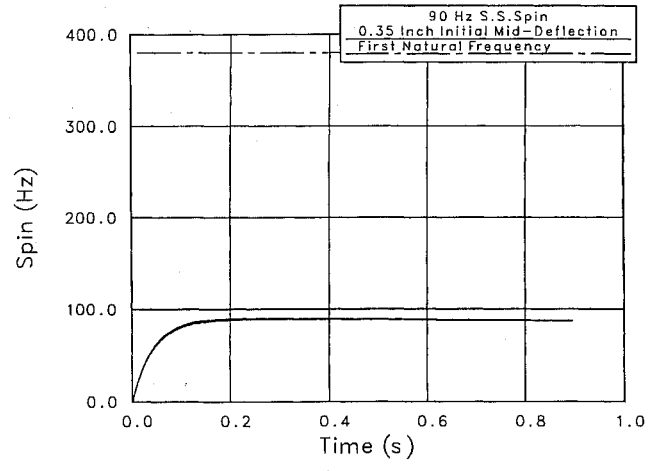

Fig. 7 Spin history, $\delta = 0.55$ deg; subcritical $p_s = 90$ Hz: 120-mm subcaliber KE projectile (steel).

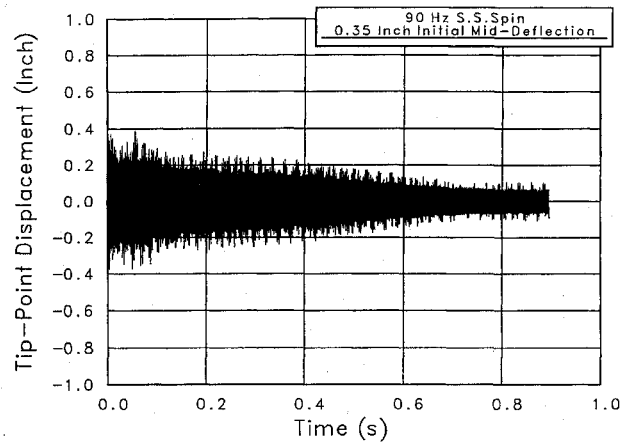

Fig. 8 Tip point deflection history, $\delta = 0.55$ deg; subcritical $p_s = 90$ Hz: 120-mm subcaliber KE projectile (steel).

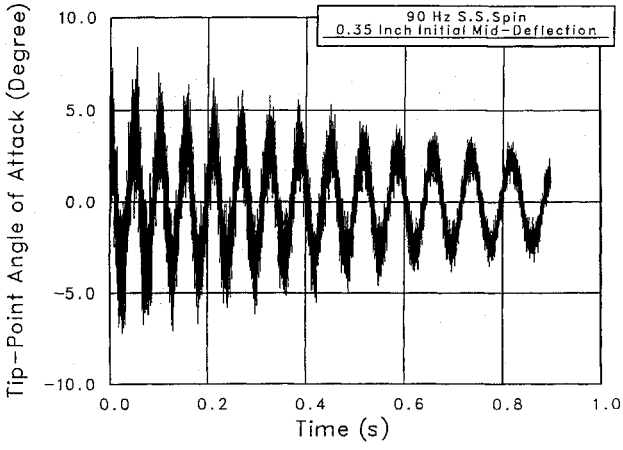

Fig. 9 Pitch angle-of-attack history, $\delta = 0.55$ deg; subcritical $p_s = 90$ Hz: 120-mm subcaliber KE projectile (steel).

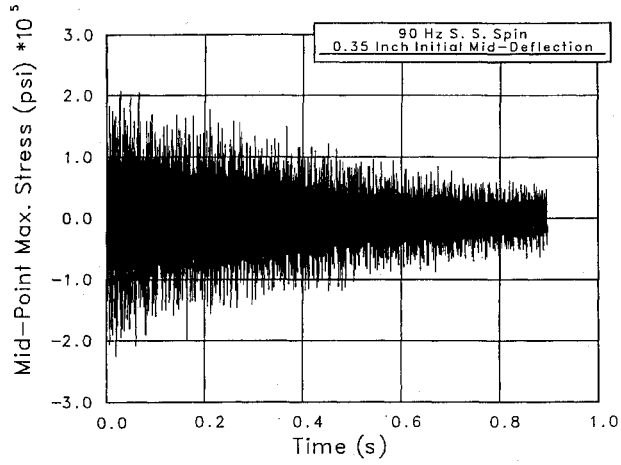

Fig. 10 Midpoint maximum stress history, $\delta = 0.55$ deg; subcritical $p_s = 90$ Hz: 120-mm subcaliber KE projectile (steel).

For spin-up cases with steady-state spin higher than the FNF, spin lock-in occurred. Figure 14 depicts the spin history for a 400-Hz case, where the rod spin locked on the value of 375 Hz, which (because of structural damping) is slightly less than the FNF of 380 Hz. The tip deflection oscillates at 0.22 in. up to $t = 0.12$ when the rod reaches a spin close to the FNF. It then quickly bends into an equilibrium shape where the forces (mainly the spin centrifugal force) are almost constant. The rod then spins at its frozen shape, at the almost constant frequency of 375 Hz. The tip deflection then reaches 0.5 in., as shown in Fig. 15. Figure 16 shows the corresponding tip point pitching angle history, reflecting an oscillation about an angle of 3.5 deg instead of the expected 0 deg. The corresponding maximum

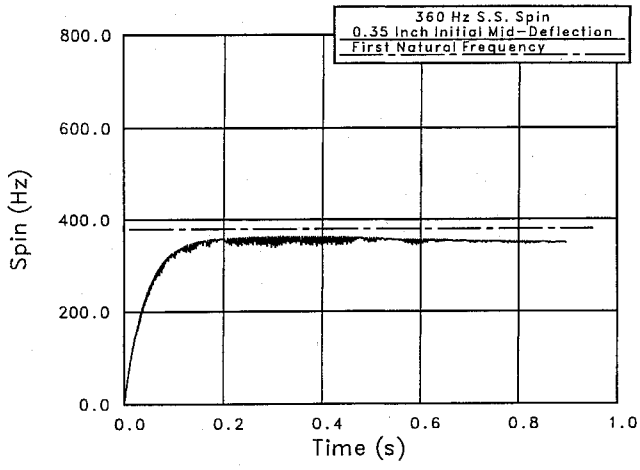

Fig. 11 Spin history, $\delta = 2.20$ deg; near critical $p_s = 360$ Hz: 120-mm subcaliber KE projectile (steel).

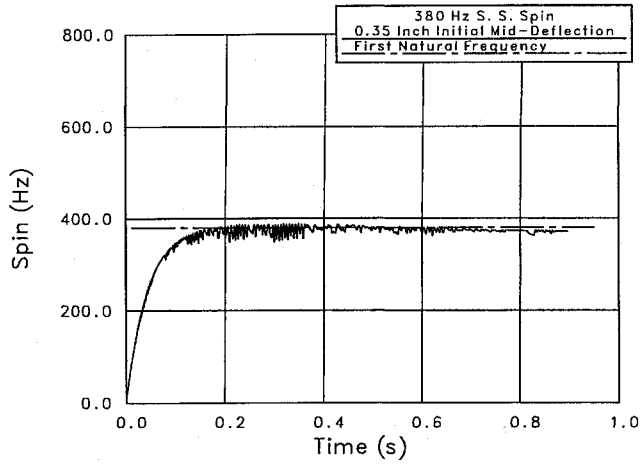

Fig. 12 Spin history, $\delta = 2.32$ deg; near critical $p_s = 380$ Hz: 120-mm subcaliber KE projectile (steel).

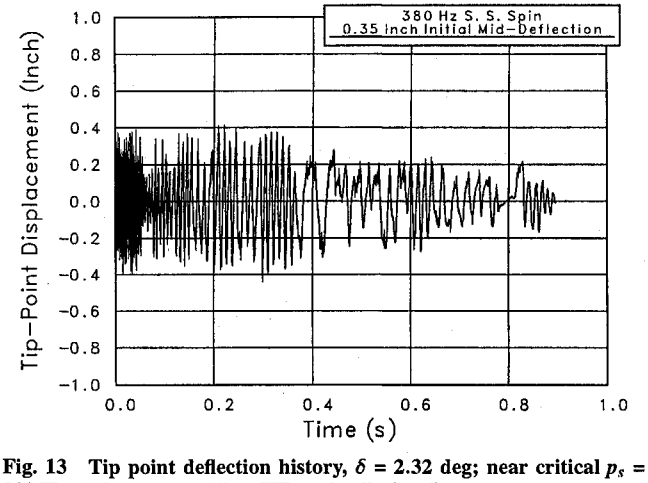

Fig. 13 Tip point deflection history, $\delta = 2.32$ deg; near critical $p_s = 380$ Hz: 120-mm subcaliber KE projectile (steel).

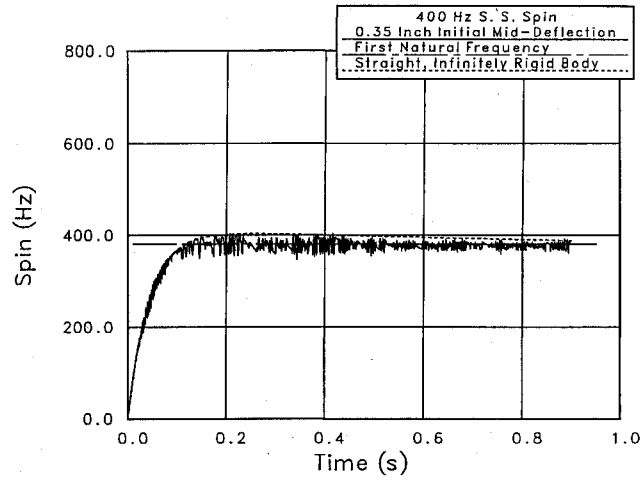

Fig. 14 Spin history, $\delta = 2.44$ deg; supercritical $p_s = 400$ Hz: 120-mm subcaliber KE projectile (steel).

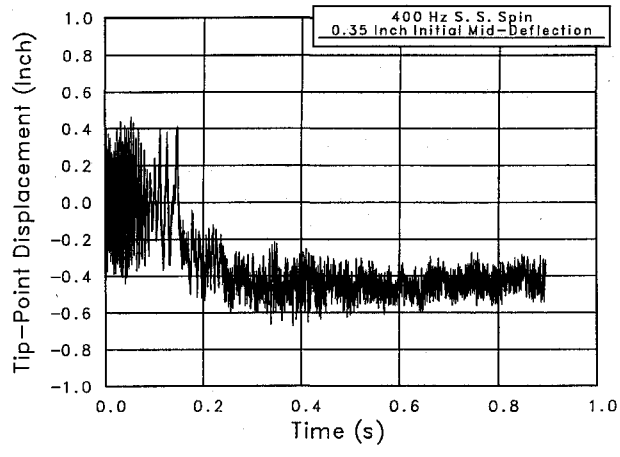

Fig. 15 Tip point deflection history, $\delta = 2.44$ deg; supercritical $p_s = 400$ Hz: 120-mm subcaliber KE projectile (steel).

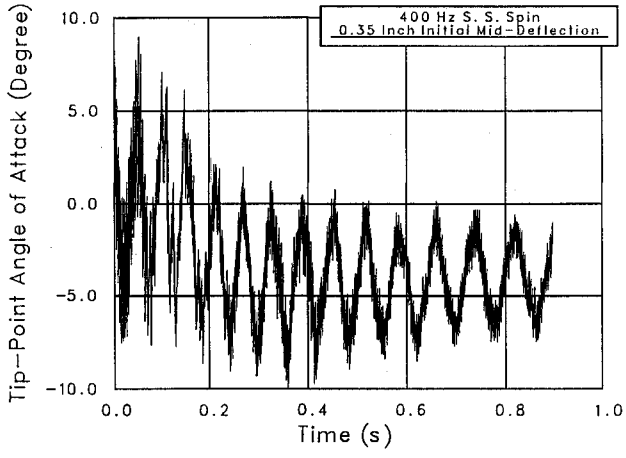

Fig. 16 Pitch angle-of-attack history, $\delta = 2.44$ deg; supercritical $p_s = 400$ Hz: 120-mm subcaliber KE projectile (steel).

stress was quite large (200,000 psi) as shown in Fig. 17. This value exceeds the static yield stress for steel and may indicate rod breakage. The same spin lock-in behavior is also shown in Fig. 18 for the case of 450 Hz. Another case of spin lock-in is the case of 720 Hz, depicted in Fig. 19. It shows spin lock-in at the 375-Hz mark instead of spinning to 720 Hz. The corresponding tip point deflection history is similar in pattern to the lock-in case of Fig. 15. The deflection is becoming considerably large, far beyond the validity of Eq. (3), even with using the large deflection correction term a. The deflection freeze is also evident in this case for the spin lock-in. Note that the rod shape, at any instant after lock-in, was similar but not identical to the first bending mode shape. The end points of the projectile deflected slightly differently, reflecting the different mass, force loading, and area moment of inertia distribution at both nose and tail ends.

The results are found to be consistent with observed firing test results of a similar penetrator, the 105-mm M900. Open range yaw card tests showed that the bent rod had the same large card imprints at both 1 and 3 km, whereas they had normal imprints up to 250 m.[15] This observation suggests that bending happens early near the muzzle (i.e., by 250 m) and then seems to freeze while the projectile continues its path without major deviation or instability to its 3-km yaw card target. These observations were affirmed by

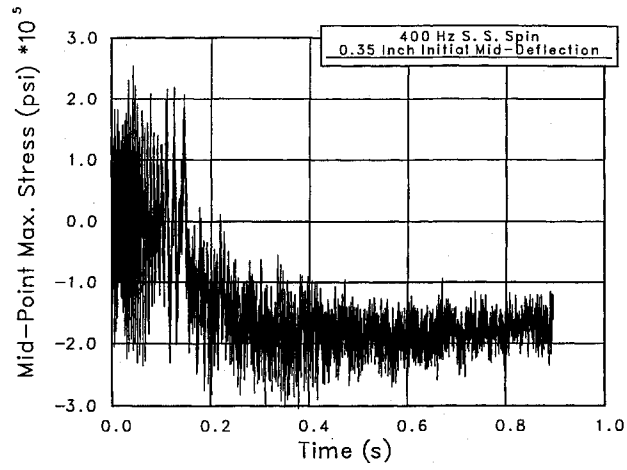

Fig. 17 Midpoint maximum stress history, $\delta = 2.44$ deg; supercritical $p_s = 400$ Hz: 120-mm subcaliber KE projectile (steel).

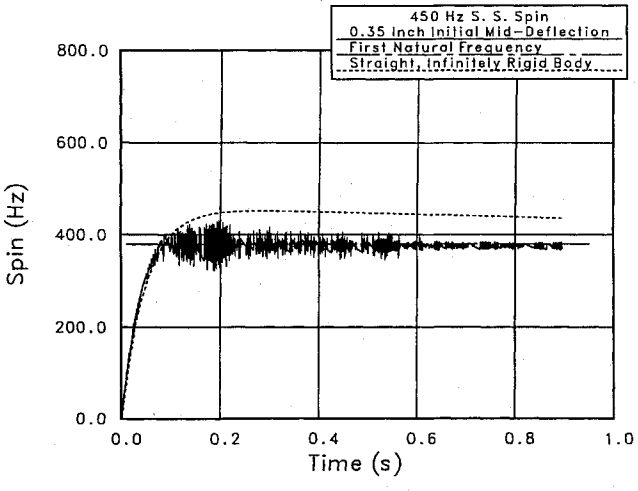

Fig. 18 Spin history, $\delta = 2.75$ deg; supercritical $p_s = 450$ Hz: 120-mm subcaliber KE projectile (steel).

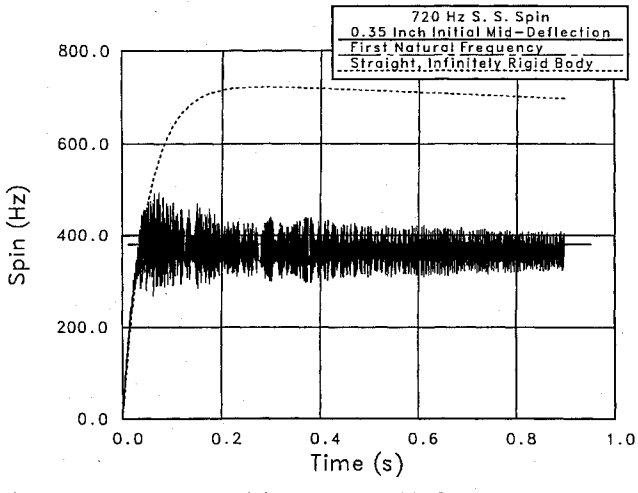

Fig. 19 Spin history, $\delta = 4.40$ deg; supercritical $p_s = 720$ Hz: 120-mm subcaliber KE projectile (steel).

the present results for the first time in the literature. Reference 3 alluded to such a behavior only for spin-pitch lock-in, but not for the spin-bend lock-in.

A spin-down case across the FNF was examined to investigate whether the rod will spin lock on the FNF while reaching its low subcritical design spin. The projectile was modeled to have been launched at 600 Hz and to have undamaged fins to achieve a subcritical steady state of 90 Hz. The result for the spin history, shown in Fig. 20, indicates unimpeded spinning down through the FNF toward the design steady-state spin. Only the transient response

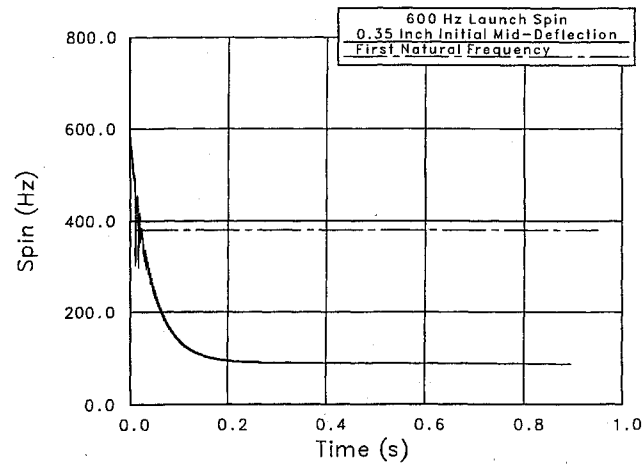

Fig. 20 Spin history, high launch spin; 600 Hz, $p_s = 90$ Hz: 120-mm subcaliber KE projectile (steel).

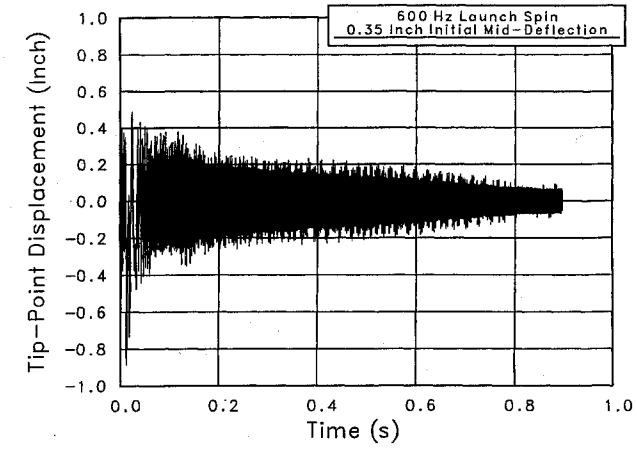

Fig. 21 Tip point deflection history, high launch spin; 600 Hz, $p_s = 90$ Hz: 120-mm subcaliber KE projectile (steel).

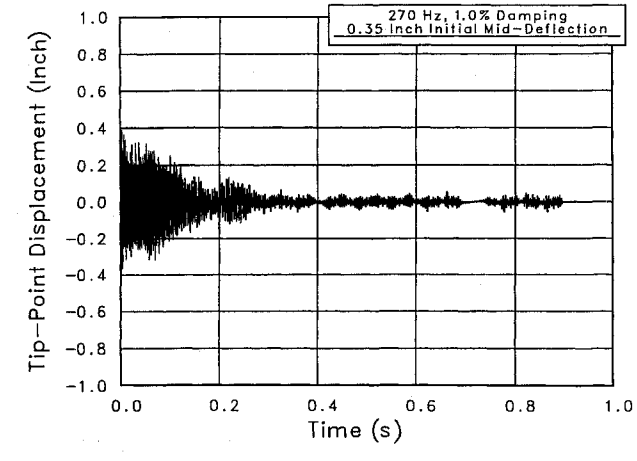

Fig. 22 Tip point deflection history, with 1.00% structural damping, $\delta = 1.65$ deg subcritical $p_s = 270$ Hz: 120-mm subcaliber KE projectile (steel).

during the crossing, as expected, shows large spin oscillations. The corresponding tip point deflection is given in Fig. 21. It indicates a large transient response because of the crossing, but then it dampens out as the projectile achieves a low spin and thus less rod deflection.

Effect of the structural damping was studied by increasing the damping coefficient c from 0.002 to 0.010 for the design spin case of 90 Hz. The spin response showed insignificant change when compared to Fig. 7. However, a large decrease in the deflection was obtained, as expected, as shown by Fig. 22 when compared to Fig. 8.

Effect of rod initial shape on spin lock-in was examined by recomputing the case of 720 Hz, starting with a second mode shape

with the same maximum rod sag of 0.35 in. This test was performed to observe whether the second mode shape will excite vibration at the second natural bending frequency and possibly escape lock-in at the FNF. The result obtained still indicated lock-in at the FNF, but with much larger spin and deflection oscillations.

Conclusions

A model was developed to simulate the structural dynamic response for a free/free penetrator in flight, subjected to both instantaneous aerodynamic and spin forces while the rod is undergoing simulated planar pitching motion. Spin, deflection, pitch angle, and maximum rod stress histories along the traveled trajectory can now be made for actual flight speeds and conditions. Results for both sub- and supercritical spin values have been obtained, as well as for the critical spin. These results indicate a spin lock-in at the first flexural natural frequency if the rod is unavoidably spun (because of damaged fins) above that natural frequency barrier. Initial rod shape was found not to interfere with this behavior, even if the initial rod shape resembled the second frequency mode shape. Also, a spin-down case from a high supercritical to a low subcritical spin value was found to escape being locked in to that frequency barrier.

The following conclusions are drawn based on the results obtained through the application of the present analysis and model.

General

1) Rod bending causes an increase in the rod axial moment of inertia about its spin axis, thus causing a trend to lower the spin from the corresponding value for the unbent rod.

2) The spin magnitude of the rod (either purposefully by design or because of damaged fins) and the existence of an initial rod deformed shape (or mass eccentricity for straight rods) are the main factors causing the spin lock-in.

Effect of Spinning Quite Below the FNF

3) A spinning long rod, elastically bent near the muzzle (because of impulse loading, huge acceleration, and in-bore dynamics), will continue in flight in a continuous flexing motion (lateral bending), while pitching and spinning, as long as the rod spin rate is below its FNF. The amplitude of the flexing will also attenuate, because of the rod structural damping.

4) The aerodynamic loading for the bent rod is dominant only for the slow spinning rods (less than 30 Hz). For high-spin rods, the spin force largely exceeds the aeroloading.

Effect of Spinning Up Near, But Below, the FNF

5) The rod will not spin lock-in at the FNF, both its spin oscillation and deflection magnitude start to be larger, then dampen out also.

Effect of Spinning Up Above the FNF

6) If the projectile fins are damaged such that to produce a high steady-state spin exceeding the FNF the bent rod will spin accelerate to that frequency and get locked in to it with an amplified rod bending deflection. However, the rod will continue its flight and almost freeze into its newly magnified bent and will not flex significantly further.

7) To escape this lock-in, the rod has to be both perfectly straight and infinitely rigid (i.e., undeformable, or $E \rightarrow \infty$).

Effect of Spinning Down Through the FNF

8) One exception for not locking into the FNF while passing through it is the case of spin down through that frequency barrier. When the bent rod was modeled to be launched from the muzzle with a spin higher than its critical frequency (e.g., when launched from a rifled tube), while the fins are assumed to be undamaged, the rod spun down to its low design spin rate without locking in to that barrier spin.

Effect of Initial Rod Shape on Spin Lock-In

9) If the spinning bent rod starts near the muzzle, with a shape that resembles the second bending mode, it still will not spin through the FNF. It will spin lock-in at that FNF frequency.

Effect of the Internal Structural Damping

10) The effect of the intrinsic structural damping was minimal on the spin response pattern but was evident on the deflection response magnitude. A case with structural damping, five times larger than the normal (i.e., 1.0% compared to 0.2% of the critical damping value for the rod), resulted in a decrease of about 50% in the magnitude of the tip point deflection of the rod.

References

[1]Stearns, B., Hathaway, W., and Whyte, B., "Flexible Body Trajectory Simulation—Preliminary Report," Arrow Tech Associates, ARROW-010-88, S. Burlington, VT, Oct. 1988.

[2]Legner, H. H., and Reinecke, W. G., "Aerodynamic Effects of In-Flight Geometry Modifications on Hypervelocity Projectiles," *Proceedings of the 14th International Symposium on Ballistics* (Quebec, PQ, Canada), Vol. 1, American Defense Preparedness Association, Arlington, VA, 1993, pp. 695–703.

[3]Legner, H. H., Lo, E. Y., and Reinecke, W. G., "On the Trajectory of Hypersonic Projectiles Undergoing Geometry Changes," AIAA Paper 94-0719, Jan. 1994.

[4]Rapacki, E. J., "In-Flight Long Rod Penetrator Bending," Presentation, U.S. Army Ballistic Research Lab., Aberdeen Proving Ground, MD, March 1986.

[5]Rapacki, E. J., private communications, U.S. Army Research Lab., Aberdeen Proving Ground, MD, Jan. 1993.

[6]Held, B., private communications, U.S. Army Research Lab., Aberdeen Proving Ground, MD, March 1993; also short computer code for determining rod spin based on its increased axial moment of inertia.

[7]Buckland, R. W., "On the In-Flight Vibration of Long Rod," Defense Research Agency, Group Working Paper 5/92 (WS2), Military Div., Fort Halstead, Kent, England, UK, March 1992.

[8]Platus, D. H., "Aeroelastic Stability of Slender, Spinning Missiles," *Journal of Guidance, Control, and Dynamics*, Vol. 15, No. 1, 1992, pp. 144–151.

[9]Clare, T. A., "Resonance Instability for Finned Configurations Having Nonlinear Aerodynamic Properties," *Journal of Spacecraft and Rockets*, Vol. 8, No. 3, 1971, pp. 278–283.

[10]Devan, L., and Mason, L. A., "Aerodynamics of Tactical Weapons to Mach Number 8 and Angle of Attack 180: Part II, Computer Program and Users Guide," Naval Surface Weapons Center, NSWC-TR-81-358, Dahlgren, VA, Sept. 1981.

[11]Jenke, L. M., "Experimental Roll-Damping, Magnus, and Static Stability Characteristics of Two Slender Missile Configurations at High Angles of Attack (0 to 90 Deg) and MACH Numbers 0.2 Through 2.5," Arnold Engineering Development Center, AEDC-TR-76-58, Arnold AFB, TN, July 1976.

[12]Blevins, R. D., *Formulas for Natural Frequency and Mode Shape*, Van Nostrand Reinhold, New York, 1979, pp. 108–113, 160–163.

[13]Morris, B., "Modal Testing of 120 mm DM13 KE Round," U.S. Army Research Lab. Site Component, Adelphi, MD, April 1994.

[14]Shelly, S. J., "Structural Flexibility, Inter-Nodal Stiffness and Global Stiffness Concept," Univ. of Cincinnati Preliminary Rept., prepared for U.S. Army Research Lab. Component, Adelphi, MD, Feb. 1994.

[15]Pennekamp, R. A., and Jara, E. A., "M900 Technical Test Results: Yaw and Spin Characterization Subtest," U.S. Army Ballistic Research Lab., BRL-MR-3941, Aberdeen Proving Ground, MD, Dec. 1991.

R. M. Cummings
Associate Editor